THE JOURNAL OF PHYSICAL CHEMISTRY C

Article

Cite This: J. Phys. Chem. C 2018, 122, 27820−27828

pubs.acs.org/JPCC

High-Pressure Evolution of Unexpected Chemical Bonding and Promising Superconducting Properties of YB_6

Jianyun Wang, Xianqi Song, Xuecheng Shao, Bo Gao,* Quan Li,* and Yanming Ma

State Key Laboratory of Superhard Materials, Key Laboratory of Automobile and Materials of MOE, and Innovation Center for Computational Physics Method and Software, Jilin University, Changchun 130012, China

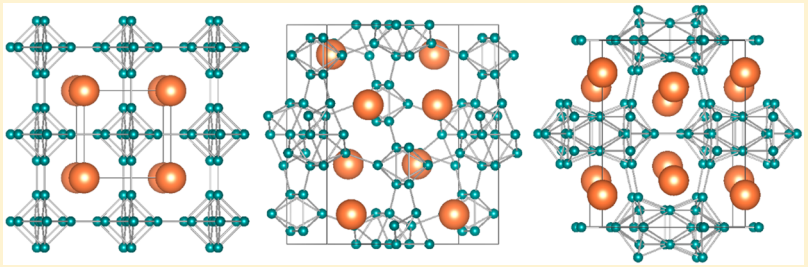

ABSTRACT: As the prototype of MB_6 (M = alkaline-earth and rare-earth metals) compounds, YB_6 possesses the highest superconducting critical temperature in this family at the ambient pressure. Here, we performed a first principle exploration on the chemical bonding states and the corresponding electronic properties of YB_6 at high pressure. Two phases with *Cmcm* and *I*4/*mmm* space groups are predicted using CALYPSO method, energetically more stable than the previously proposed structures. The B covalent network is eventually evolved from B_6 octahedron in the cubic *Pm*-3*m* phase to B_{24} unit in *I*4/*mmm* phase. The calculated electron−phonon coupling parameters show that the contribution of B is significantly increased by the high-pressure effect in *Cmcm* and *I*4/*mmm* structure, contrary to that in *Pm*-3*m* structure. Further calculations of electron−phonon coupling indicate that the high-pressure phases are likely superconducting with the major contribution by boron phonon vibration.

1. INTRODUCTION

The metal hexa-borides (MB_6) crystallized in the cubic CsCl structure have received considerable attention, due to their fundamental and technological importance.[1−3] The metal elements in the MB_6 family mainly belong to alkaline-earth (Ca, Sr, and Ba) and rare-earth metals (Y, La, and Ce). For alkaline-earth-metal hexa-borides, they show semiconductivity and exhibit unusual weak ferromagnetic-like properties.[4−6] The rare-earth metal hexa-borides have a wide range of unusual physical properties, including heavy Fermion in CeB_6,[7] ferromagnetic characteristics in EuB_6,[8] Kondo semiconducting properties in SmB_6,[9,10] and topological insulator states in YbB_6.[11,12] Therefore, the rare-earth hexa-borides have attracted great interest and been studied widely in the past decades.

Since the discovery of the highest superconducting critical temperature (T_c; ∼39 K) in conventional superconductors under ambient pressure in MgB_2,[13−16] the metal borides are investigated extensively to design new potential high-temperature conventional superconductors. As one of rare-earth hexa-borides, YB_6 has superconducting properties with the highest T_c (1.5−8.4 K) in the MB_6 family. Several theoretical and experimental studies have contributed to the understanding of the fascinating properties of YB_6, including the charge fluctuation using optical excitation measurements, and specific heat, resistivity, Hall and Seebeck coefficients, magnetization, hydrostatic density, and thermal expansion data based on the phonon density of states DOS.[17,18] High pressure has a significant effect on modulating electronic band structures and dynamic properties, as well as superconducting states.[19−23] To explore the inherent physical mechanism for superconductivity in YB_6, Xu et al.[24] have performed systematic electron−phonon coupling (EPC) calculations and demonstrated that the superconductivity of YB_6 mainly originates from the low-lying phonon frequency of the Y atom. The EPC becomes weak with the increase of pressure stemming from the hardening of the Y phonon frequency. Sluchanko et al. reported that the amount of vacancies at yttrium and boron sites can enhance the superconductivity.[25] Besides, it is well-known that the pressure can improve the electron−phonon coupling or regulate the T_c.[26] One of Y hydrides, YH_{10}, is predicted as a room-temperature superconductor with a T_c of up to 303 K at 400 GPa.[27] Therefore, the investigation of high-pressure phase and superconductivity of YB_6 is highly desirable.

As the prototype of the MB_6 family, YB_6 is crystallized with CsCl-type structure and *Pm*-3*m* space group under ambient-pressure. Recently, the high-pressure structures of alkaline-metal hexa-borides (CaB_6 and BaB_6) have been synthesized using a diamond anvil cell combined with an ab initio structural search.[28,29] The structure will undergo phase

Received: August 17, 2018
Revised: November 13, 2018
Published: November 19, 2018

DOI: 10.1021/acs.jpcc.8b08017
J. Phys. Chem. C 2018, 122, 27820−27828

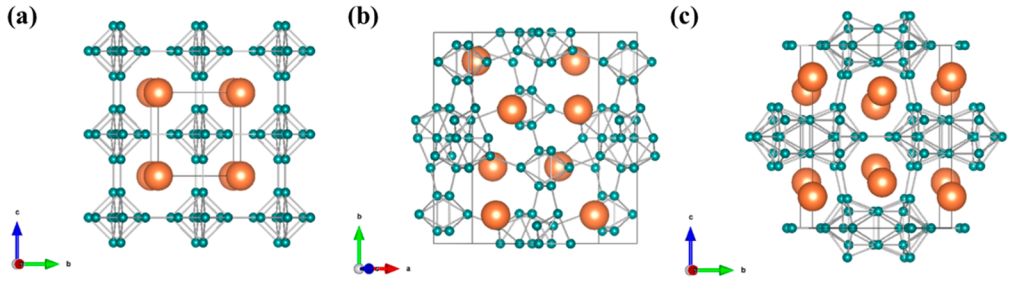

Figure 1. Optimized crystal structures: (a) *Pm*-3*m*, (b) *Cmcm*, and (c) *I*4/*mmm*. The large orange and small green balls represent Y and B atoms, respectively.

transitions accompanied by the evolution of B unit from 6-atoms to 24-atoms under pressure. However, these high-pressure phases do not show superconductivity based on the calculated EPC parameter. For LaB_6, a phase transition from cubic *Pm*-3*m* to orthorhombic *Pban* induced by the lattice distortion was observed in the experiment under high pressure.[30] However, lack of a systematic investigation on the structural evolution for YB_6 precludes the full understanding of its corresponding physical and chemical properties at high pressure.

In the current manuscript, we present a comprehensive study of pressure-induced structure transition of YB_6 over the pressure range of 0−60 GPa using the CALYPSO structure prediction approach. Two phases with *Cmcm* and *I*4/*mmm* space groups have been predicted, which are energetically more stable at the pressure range of 3.2−35.8 GPa and above 35.8 GPa, respectively. The covalent network configuration for B atom is evolved with the increase of pressure, in which B_6 octahedra in *Pm*-3*m* aggregate and transform into a B_{24} framework in *I*4/*mmm*. Volume and bond length, electronic density of states, phonon spectrum, and charge transfer for three phases are calculated to understand their electronic and dynamic properties. The analysis of bond length shows that the Y−Y and Y−B bonds in the currently predicted *Cmcm* and *I*4/*mmm* phases are shorter, while the B−B bond is evidently longer than those in the cubic phase at the same compression conditions. The calculated results suggest that the *I*4/*mmm* phase has the higher *T*c compared with the *Pm*-3*m* phase at the same pressure, and the T_c values of three phases are slightly decreased with the increase of pressure due to the hardening of phonon. The T_c are 7.47 K at 0 GPa, 2.00 K at 5 GPa, and 3.75 K at 37 GPa for *Pm*-3*m*, *Cmcm*, and *I*4/*mmm* under their stable pressure range, respectively.

2. COMPUTATIONAL METHODS

The structural search for YB_6 was performed by swarm-intelligence-based CALYPSO method,[31,32] which can effectively explore the multidimensional potential energy surface and requires no prior structure information.[33,34] The CALYPSO method has been benchmarked on a variety of known systems and successfully predicted the ground-state structures of various systems ranging from elemental solids to binary and ternary compounds.[35−44] The structural search was carried out with simulation cell sizes of 1−4, 6, and 8 formula units (f.u) at 0, 20, 40, and 60 GPa. In each prediction, the population size in a generation is set to 50. The proportion of the structures generated by particle swarm optimization is 60%. The rest of the structures are then randomly generated with symmetry. A total of 20−40 generations are performed to reach the criterion of convergence. When the predicted stable structure is not evolved after five generations, the prediction reaches the criterion of convergence. To search the potential energy landscape sufficiently, several individual predictions have been performed for the cell sizes with 4, 6, and 8 f.u. More than 2500 configurations are sampled for each predictions of the cell sizes with 4, 6, and 8 f.u. All prediction structures have been classified and checked by our SPAP program,[45] in which the coordination characterization function is used to assess structural similarity, and the similarity of structures have been eliminated. The calculated energy evaluation, structural optimization and electronic properties were performed in the framework of density functional theory as implemented in the VASP (Vienna Ab Initio simulation package) code,[46] described by projector-augmented wave (PAW) method,[47,48] where $5s^24d^{11}$ and $2s^22p^1$ electrons were taken as the valence electrons for Y and B atoms, respectively. The generalized gradient approximation of Perdew, Burke, and Ernzernhof (GGA-PBE) is adopted for the exchange correlation functional.[49] The plane-wave kinetic energy cutoff of 700 eV and a Monkhorst−Pack[50] K-spacing of $2\pi \times 0.03$ Å^{-1} in reciprocal space were chosen to ensure that total energy are converged to less than 1 meV/atom. The phonon dispersion is calculated based on the finite displacement method using a supercell approach[51] in Phonopy software.[52] Bader's quantum theory of atoms in molecules analysis was adopted for the charge-transfer analysis.[53] EPC calculation is explored by plane-wave pseudopotential method and density-functional perturbation theory, as implemented in the Quantum-ESPRESSO package.[54] The kinetic energy was used with a tested value of 70 Ry. A 6 × 6 × 6 MP *q*-point mesh with a 12 × 12 × 12 MP *k* mesh for *Pm*-3*m*, a 4 × 4 × 4 MP *q*-point mesh and 8 × 8 × 8 MP *k* mesh for *Cmcm* phase, and a 5 × 5 × 5 MP *q*-point mesh and 10 × 10 × 10 MP *k* mesh for *I*4/*mmm*, were chosen to ensure k-point sampling convergence.

3. RESULTS AND DISCUSSION

The previously known CsCl-type *Pm*-3*m* structure [Figure 1a] was successfully reproduced at ambient pressure, confirming the reliability of our calculations. The optimized crystal structure information on the *Pm*-3*m* phase is shown in Table 1, in good agreement with the previously calculated and experimental data. Six B atoms form the octahedron units, and Y atom and B_6 unit locate at Cs and Cl sites in a unit cell, respectively. The calculated enthalpies per chemical formula unit of predicted low-energy structures with respect to the *Pm*-3*m* structure at the pressure range 0−60 GPa are plotted in Figure 2. At high pressure, two high-pressure phases were uncovered whose structure information are tabulated in Table 1, including two metastable phases (*Cmmm* and $P6_3mc$). It is

DOI: 10.1021/acs.jpcc.8b08017
J. Phys. Chem. C 2018, 122, 27820−27828

Table 1. Optimized Structural Parameters for YB_6

space group	pressure (GPa)	lattice parameters (Å)	atom coordinates (fractional)
Pm-3*m*	0	$a = b = c = 4.0984$	Y1 1a (0.1998,0.0,0.0)
			B1 6f (0.0, 0.0, 0.0)
Cmcm	5	$a = 8.6705$, $b = 10.4126$,	Y1 8g (0.2945,0.3649,0.25)
		$c = 5.5553$	B1 8f (0, 0.0600, 0.4069)
		$\alpha = \beta = \gamma = 90°$	B2 8f (0,0.2266,0.4087)
			B3 8f (0, 0.3586, 0.9175)
			B4 8f (0.0, 0.0, 0.5966)
			B5 8g (0.6462, 0.6391, 0.25)
			B6 8g (0.8337, 0.5847, 0.25)
*I*4/*mmm*	37	$a = b = 6.7480$,	Y1 4e (0.5,0.5,0.6730)
		$c = 8.8241$	Y2 4d (0.5,0.0,0.25)
		$\alpha = \beta = \gamma = 90°$	B1 16n (0.5, 0.3036,0.9086)
			B2 16i (0.3789,0.8000,0.5)
			B3 16m (0.2745,0.2745,0.1604)
Cmmm	30	$a = 8.4718$, $b = 6.8070$,	Y1 4g (0.2986,0.5,0)
		$c = 3.8725$	B1 4h (0.4062,0,0.5)
		$\alpha = \beta = \gamma = 90°$	B2 8n (0,0.3051,0.2055)
			B3 4j (0,0.1182,0.5)
			B4 8q (0.1576,0.72411,0.5)
$P6_3mc$		$a = b = 4.7478$,	Y1 2b (0.3333,0.6667,0.8155)
		$c = 5.2385$	B1 6c (0.1154,0.8846,0.1178)
		$\alpha = \beta = \gamma = 90°$	B2 6c (0.2044,0.7956,0.4100)

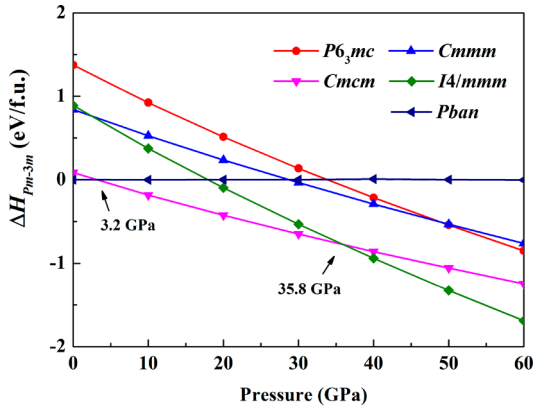

Figure 2. Relative enthalpy per formula unit referenced to CsCl-type (*Pm*-3*m*) phase for competing structures as a function of pressure from 0 to 60 GPa.

found that the evolution of structure and B covalent network is consistent with that in the CaB_6 system under high pressure[28] but different from LaB_6 and BaB_6.[29,30] An orthorhombic phase [Figure 1b] with the space group of *Cmcm* (8 f.u/cell) is found to become energetically stable above 3.2 GPa. In the *Cmcm* structure, half of B_6 octahedra collapses and opens up to form zigzag strips, accompanied by a distortion of the remaining B_6 octahedra and Y atoms under compression. With the increase in pressure, we identify a tetragonal *I*4/*mmm* (8 f.u./cell) [Figure 1c] phase, which become energetically more stable than the *Cmcm* phase at 35.8 GPa. All B_6 octahedral units collapse and form the 24-atom B unit with three others in *I*4/*mmm* structure. We also consider the stability of the *Pban* phase proposed in a previous LaB_6 study.[30] The calculated difference of enthalpy for *Pm*-3*m* and *Pban* phases is below 2 meV/f.u. in the pressure rang from 0 to 60 GPa, suggesting that both phases are energy-degenerate.

To assist the further experimental identification, the structural assignments for YB_6, we have shown the calculated frequencies of Raman modes and X-ray diffraction (XRD) data for pure *Pm*-3*m*, *Cmcm*, and *I*4/*mmm* at 0, 5, and 40 GPa, respectively [Figure 3]. Our results show that the calculated Raman peak positions of the *Pm*-3*m* phase at ambient conditions are in excellent agreement with experimental data. The calculated frequencies of T_{2g}, Eg, and A_{1g} of *Pm*-3*m* phase are 706.1, 1188.3, and 1328.5 cm^{-1}, respectively, which are in good agreement with experimental observation (e.g., T_{2g} at 706 cm^{-1}, E_{1g} at 1205 cm^{-1}, and A_{1g} at 1320 cm^{-1})[55,56] From the measured Raman spectrum, the ambient structure is dominant up to 9[56] and 14 GPa,[57] where the *Cmcm* structure is theoretically well established as the thermodynamically stable phase, as shown in Figure 2. Therefore, there are large enthalpy barriers between these phases that cannot be easily overcome at experimental (room) temperature.[56,57]

As shown in Figure 4, the variation of volumes and average bond lengths of Y−Y, B−B, and Y−B for *Pm*-3*m*, *Cmcm*, and *I*4/*mmm* phases at pressure ranging from 0 to 60 GPa. The volumes and bond lengths of three phases are decreased with the increase of pressure. The relationship of volume for three phases is *Pm*-3*m* > *Cmcm* > *I*4/*mmm* at the same pressure because of the aggregation of B_6 octahedron in *Cmcm* and *I*4/*mmm* structures. The recent experimental Raman observation[58] and theoretical calculations[58,24] show that the shorten Y−Y bonds for the *Pm*-3*m* phase will be accompanied by the soften phonon modes and reduced symmetry. For the bonds of Y−Y and Y−B, the relationship of three phases is consistent with volume, in which *Cmcm* and *I*4/*mmm* have shorter bonds compared with *Pm*-3*m* phase. Especially, the shorter Y−B bonds in *Cmcm* and *I*4/*mmm* phases may induce a stronger interaction between Y and B. For the B covalent network, the interpolyhedral bonds are shorter than intrapolyhedral bonds in three phases, indicating the interpolyhedron bonds are stronger than intrapolyhedral bonds. Different with the relationship of volume, and Y−Y and Y−B bond, both interpolyhedral and intrapolyhedral B−B bonds in the high-pressure *Cmcm* and *I*4/*mmm* phases are longer than that in *Pm*-3*m* phase. The longer B−B bond may weaken the interaction between two B atoms. Note that the B−B interoctahedral bond in *Cmcm* phase is shorter than the bond between B_6 and B strip, while still longer than the bonds in *Pm*-3*m* phase. Previous study of alkaline-earth hexaborides found that the *Cmcm* phase is more stable when B−B interoctahedral bond is longer than that in *Pm*-3*m* phase.[59] Our results prove that this rule is also applicable in YB_6, and the transition pressure from *Pm*-3*m* to *Cmcm* phase in YB_6 (3.2 GPa) is much lower than that in CaB_6 (13.0 GPa).

In the *Pm*-3*m* phase, the interoctahedron B−B bonds form σ bonds and intraoctahedron B−B bonds are connected with τ bonds.[60,61] From the calculated charge density and electron localization function plots [not shown], the σ bonds are much stronger than these τ bonds. The phase transition from *Pm*-3*m* to *Cmcm* phase is accompanied by the collapse of half the B_6 octahedrons and bonding into connected chains. The

DOI: 10.1021/acs.jpcc.8b08017
J. Phys. Chem. C 2018, 122, 27820−27828

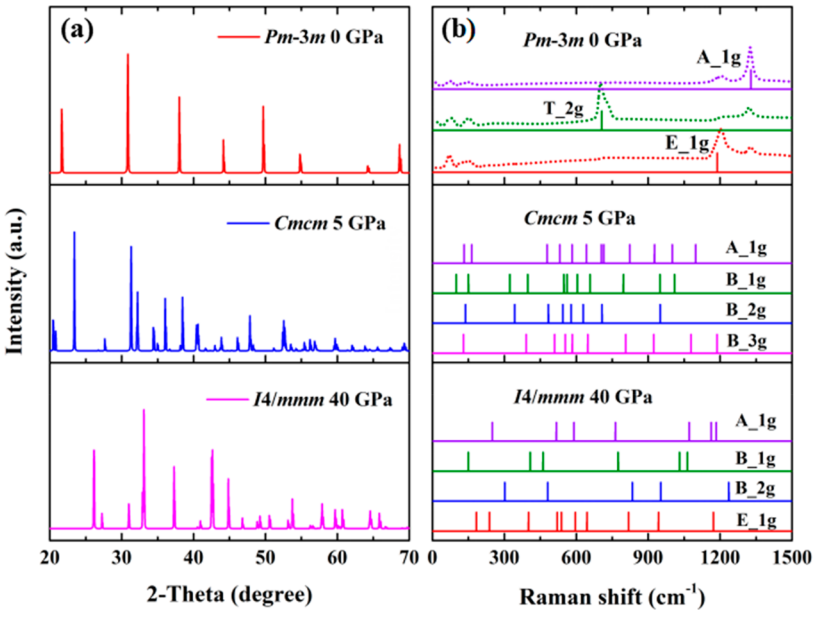

Figure 3. Simulated X-ray diffraction (a) and Raman spectra (b) for YB_6. The previous Raman data[55] at ambient conditions have been shown for comparison.

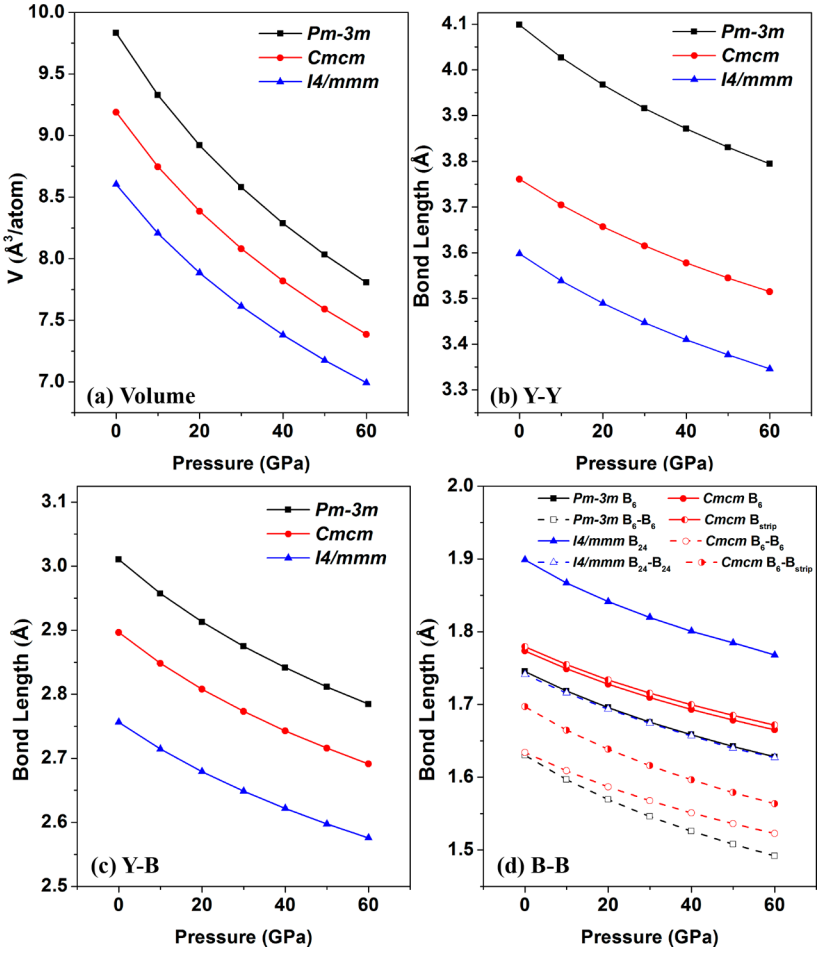

Figure 4. Calculated volume (a), average Y−Y (b), Y−B (c), and B−B (d) bond lengths of *Pm*-3*m*, *Cmcm*, and *I*4/*mmm* phases as a function of pressure from 0 to 60 GPa.

exploration of the bond breaking, collective, and rebonding process for these phases to evaluate the corresponding kinetic barriers at high pressure will offer critical insights into the underlying mechanisms for phase stability and transformation at atomic scale.[19,62] The previous Raman experiments show that there are large enthalpy barriers between these phases that

DOI: 10.1021/acs.jpcc.8b08017
J. Phys. Chem. C 2018, 122, 27820−27828

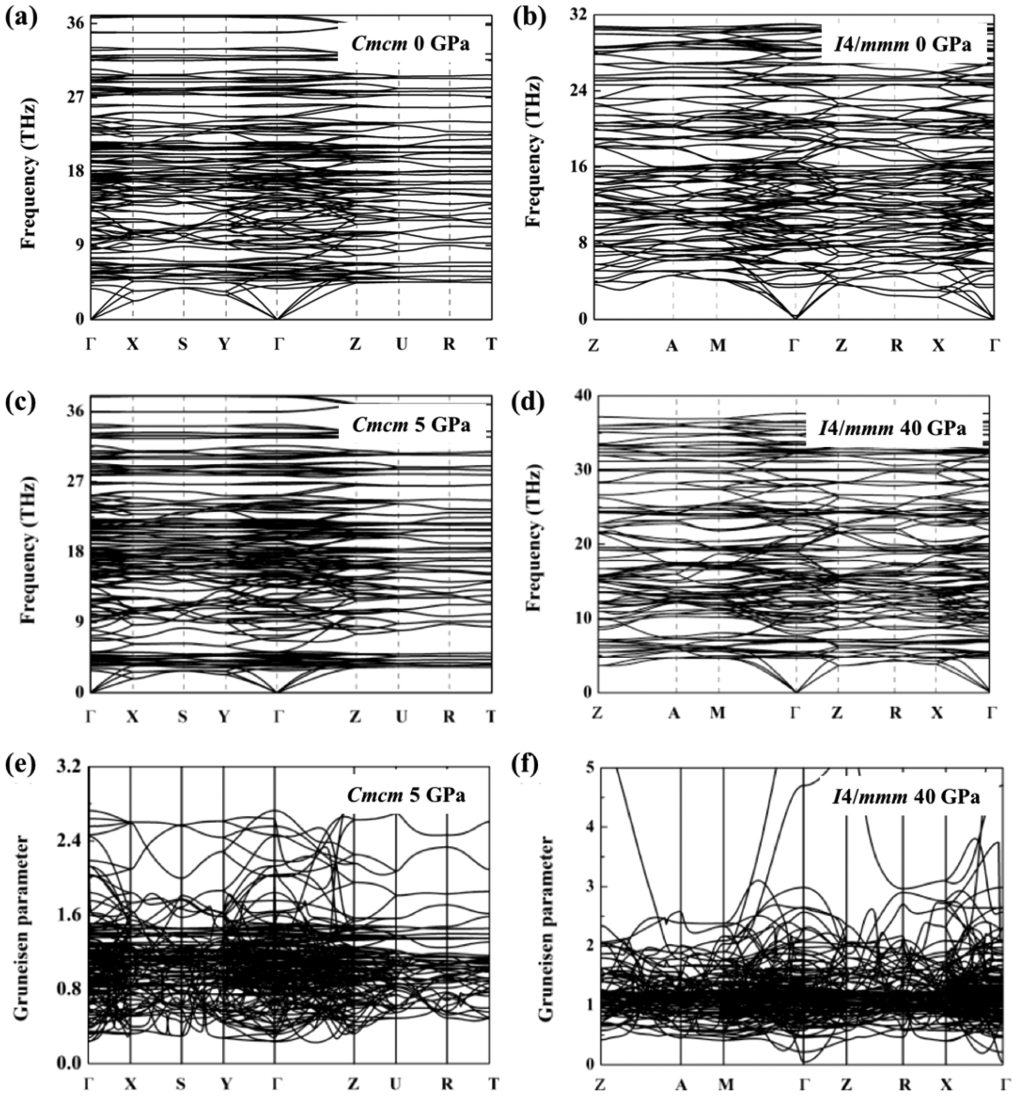

Figure 5. Calculated phonon-dispersion curves for (a) *Cmcm* at 0 GPa, (b) *Cmcm* at 5 GPa, (c) *I*4/*mmm* at 0 GPa, and (d) *I*4/*mmm* at 40 GPa. Calculated mode Gruneison parameters for (e) *Cmcm* at 5 GPa and (f) *I*4/*mmm* at 40 GPa.

hinder the occurrence of phase transitions.[56,57] The transition process for the boride are sophisticated due to the rich variety of transition pathways between these phases, and these calculations are beyond the scope of this work. We hope that the current results will stimulate further theoretical or experimental explorations on the intriguing bonding evolution and kinetic barrier calculations.

The phonon dispersion curves of three stable structures were calculated and presented in Figure 5a–d. The mode Grüneisen parameters of *Cmcm* and *I*4/*mmm* phases are calculated and depicted in the Figure 5e,f. The results show that there is no imaginary frequency in the phonon dispersion curves from ambient pressure to their stable pressure (5 GPa for *Cmcm* and 40 GPa for *I*4/*mmm*), suggesting the dynamical stability of these three phases. Previous calculation showed that there is a small gap between acoustic and optical modes in the phonon of *Pm*-3*m* phase at 0 GPa.[24] According to the calculated projected phonon density of states [Figure 7], the acoustic and optical modes are mainly from the Y and B vibrations, respectively. It is interesting to note that there is no clear gap between acoustic and optical modes in the phonon spectra of high-pressure *Cmcm* and *I*4/*mmm* phases. For the two high-pressure phases, the interatomic distances of Y–B are observably shorter these of *Pm*-3*m* phase, while the B–B bond lengths become longer [Figure 4], indicating the covalent interactions between Y and B atoms are much enhanced. This special physical behavior makes the vibrational hardening and softening of Y and B atoms, respectively, and closes the gaps between the acoustic and optical modes for the high-pressure phases. The calculated mode Gruneison parameters show the positive values, suggesting that the phonon frequencies of *Cmcm* and *I*4/*mmm* phases are predicted to have a positive pressure dependence with the increasing pressure and demonstrating that the increase of pressure can enhance the kinetic stability of *Cmcm* and *I*4/*mmm* phases. Previous calculation suggests that the phonon of *Pm*-3*m* soften to zero frequency at about 54.5 GPa, which will induce a phase transition.[24] Note that the pressure of transition from *Pm*-3*m* to *Cmcm* phase is 3.2 GPa, which is much lower than the pressure of phonon softening of *Pm*-3*m*. Such a big difference suggests that the phase transition is not directly induced by the phonon softening behavior, and the soft-mode phase transition is hidden by the transition to the *Cmcm* phase.

DOI: 10.1021/acs.jpcc.8b08017
J. Phys. Chem. C 2018, 122, 27820–27828

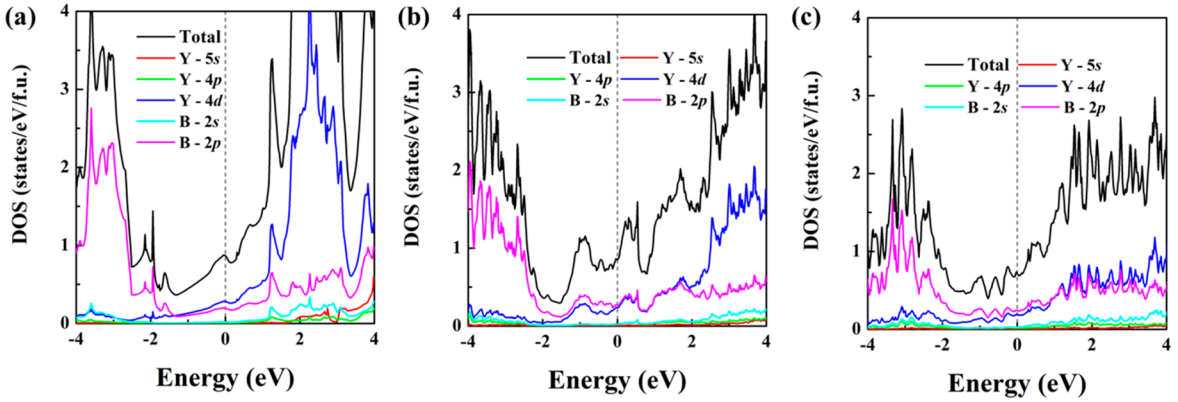

Figure 6. Calculated total and partial DOS of (a) *Pm*-3*m* at 0 GPa, (b) *Cmcm* at 5 GPa, and (c) *I*4/*mmm* at 37 GPa. The Fermi level is at zero and represented using dashed line.

To understand the electronic properties of *Pm*-3*m*, *Cmcm*, and *I*4/*mmm*, the partial densities of states (PDOS) were calculated at their stable pressure as shown in Figure 6. Three phases all exhibit the metallic behavior, and the Fermi level is dominated by Y 4d and B 2p orbitals. Note that the densities of states at the Fermi level of three structures are not located at minimum states like that in CaB_6 because Y has one more valence electron than the Ca atom, indicating three YB_6 phases have large densities of states at Fermi level compared with CaB_6. The values of densities of states at Fermi level are shown in Table 2. Under ambient pressure, the densities of states at Fermi level in *Cmcm* and *I*4/*mmm* phases are slightly lower than the value in *Pm*-3*m* states. As the pressure increases, the density of states at Fermi level have a negative pressure dependence for both *Pm*-3*m* and *I*4/*mmm* phases, but with a positive dependence for the *Cmcm* phase.

Table 2. Calculated DOSs at Fermi Level (N_{Ef}), Logarithmic Average Frequency (ω_{log}), EPC Integral (λ), and Superconducting Critical Temperature (T_c) for *Pm*-3*m* at 0 and 40 GPa, *Cmcm* at 0 and 5 GPa, and *I*4/*mmm* at 0 and 37 GPa

	N_{Ef} (states/eV/f.u.)	ω_{log} (K)	λ	T_c (K)
Pm-3*m* (0 GPa)	1.36	72.31	0.87	7.47
Pm-3*m* (40 GPa)	0.41	254.92	0.77	1.27
Cmcm (0 GPa)	0.41	324.75	0.73	1.75
Cmcm (5 GPa)	0.45	268.15	0.85	2.00
*I*4/*mmm* (0 GPa)	0.86	502.52	0.73	12.78
*I*4/*mmm* (37 GPa)	0.45	234.78	0.72	3.75

The Bader charge analysis has been employed to characterize the charge transfer between Y and B. For YB_6 stable phases, B covalent networks are electron-deficient, and two electrons are transferred from one Y atom to B covalent networks to fill the intrabonding orbital. The calculated electron-transfer from Y to B in *Pm*-3*m* at 0 GPa is about 1.8 *e*, in reasonable agreement with Wade's rule. Previous calculation[12] of charge transfer from Y to B for *Pm*-3*m* structure based on Mulliken effective charges is above 2.0 *e*, which is larger than the Bader results, in agreement with the fact that the Bader method usually slightly underestimates transferred charge. The calculated electron-transfer from Y to B for *Cmcm* at 5 GPa and *I*4/*mmm* at 37 GPa are 1.74 and 1.70 *e*, respectively, which is slightly decreased compared with *Pm*-3*m* phase. The major reason is that the B−B bond in *Cmcm* and *I*4/*mmm* is much longer than that in the *Pm*-3*m* phase.

We have further performed the calculation of electronic-phonon coupling to investigate the superconductivity of the currently predicted high-pressure phases. The Eliashberg spectral function $\alpha^2F(\omega)$ and the electron−phonon integral

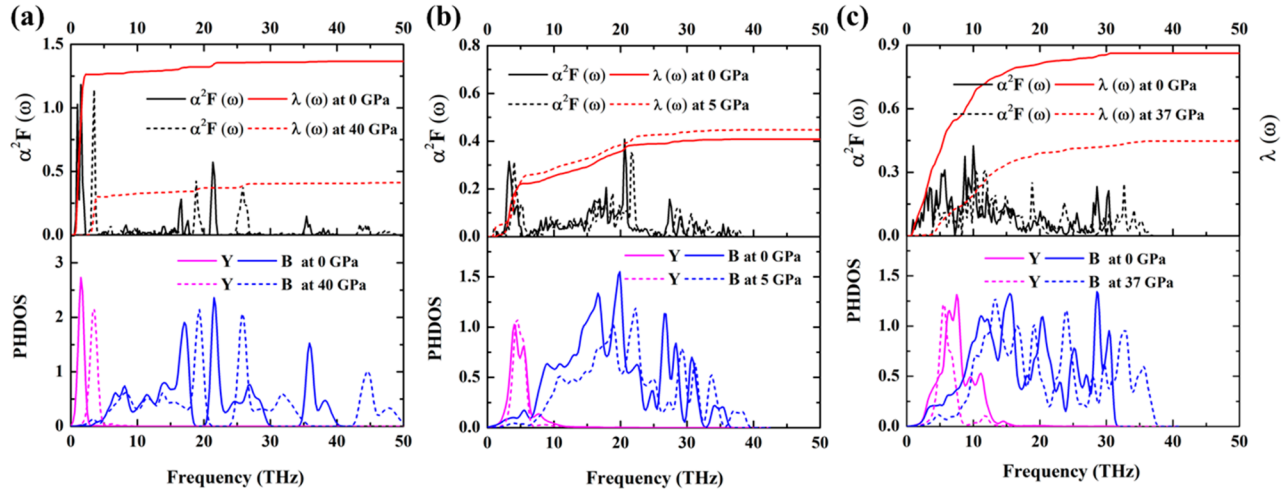

Figure 7. Calculated projected phonon density of states (lower panels), Eliashberg EPC spectral function $\alpha^2F(\omega)$ and integration $\lambda(\omega)$ (upper panels) for (a) *Pm*-3*m* at 0 and 40 GPa, (b) *Cmcm* at 0 and 5 GPa, and (c) *I*4/*mmm* at 0 and 37 GPa.

DOI: 10.1021/acs.jpcc.8b08017
J. Phys. Chem. C 2018, 122, 27820−27828

$\lambda(\omega)$ as a function of frequency ω for three phases at ambient and high pressure are shown in Figure 7. The value of λ is listed in Table 2. For *Pm*-3*m* phase at 0 GPa, the electron−phonon integral is mainly contributed by the low-lying frequencies of Y at 2.0 THz (86%) [Figure 7a], which agrees with the previous calculations. Interestingly, for the *Cmcm* phase, the proportion of low-frequency Y vibration in λ is decreased from 86% to 58% compared with the *Pm*-3*m* phase, while the proportion of B phonons is increased from 14% to 42%. We found that the peak of Y phonons locates at about 5 THz in the *Cmcm* phase, which is higher than the value in the *Pm*-3*m* phase (2 THz). This is induced by the smaller bond length between two Y atoms in the *Cmcm* phase, which enhance the force constants and make the phonon hardening. The contribution of B phonons for $\lambda(\omega)$ is mainly from the midlying part (6−22 THz), which is associated with the wagging and bending mode of B atoms. For the *I*4/*mmm* phase, the frequency of Y phonons has a larger dispersion, the peak becomes higher to reach about 7 THz, and the B phonons become soft because of the larger B−B bond length compared with the *Pm*-3*m* phase. The Y and B modes are mixed with each other, which is similar to that in oP10-FeB_4 structure.[63] The contribution of this low-frequency Y and B vibration (<15 THz) for λ is about 80%.[22] Thus, the origin of T_c in the high-pressure structure from mixed Y−B contributions is different from the superconducting mechanism of *Pm*-3*m* with Y-stretching vibrations. The λ for *Pm*-3*m*, *Cmcm*, and *I*4/*mmm* phases are 1.36, 0.41, and 0.86 at 0 GPa, respectively. With the increase of pressure, λ for *Pm*-3*m* and *I*4/*mmm* phases decrease because of the phonon hardening of Y and B. Specially, λ for the *Cmcm* phase is slightly increased to 0.45 at 5 GPa, which may be induced by the higher electronic state at Fermi level. For the high-pressure phases, the B−B bond lengths are larger than that in the *Pm*-3*m* phase at the same compressive conditions, which can weaken the B−B interaction and soften the phonons of B vibrations. In principle, the phonon branches with low-lying optical modes from week B−B bonds are beneficial to the electron−phonon coupling constant and thus the superconductivity.[64] However, the contribution for λ by the vibration of Y atoms is significantly decreased by the hardening phonons. Our theoretical results show that this competitive behavior does not effectively enhance the superconducting critical temperatures for YB_6, which have even been reduced for the *Cmcm* phase. The superconducting T_c is evaluated through the Allen-Dynes modified McMillan equation, by the calculated logarithmic average frequency ω_{log}, Coulomb pseudopotential parameters μ^*, and EPC integral λ. The calculated values of ω_{log} and T_c are shown in Table 2. Using typical μ^* of 0.1, the estimated T_c values are about 7.47, 1.75, and 12.78 K for *Pm*-3*m*, *Cmcm*, and *I*4/*mmm* at 0 GPa, respectively. The T_c of *I*4/*mmm* phase is higher than the value of *Pm*-3*m* phase because the ω_{log} of *I*4/*mmm* (502.52 K) is evidently larger than the value of *Pm*-3*m* (72.31 K) at 0 GPa. The calculated T_c of *Pm*-3*m* and *I*4/*mmm* phases are 1.27 K at 40 GPa and 3.75 K at 37 GPa, stemming from the fact that EPC integral λ is significantly decreased with the increase of pressure. Especially for *Cmcm*, the T_c is 2.00 K at 5 GPa, which is larger than the value at 0 GPa due to the large λ.

4. CONCLUSIONS

In summary, we have systematically investigated the phase stability and superconductivity of YB_6 under the pressure ranging from 0 to 60 GPa. Two high-pressure phases (*Cmcm* and *I*4/*mmm*) have been predicted by CALYPSO structure prediction method. They were found to be energetically more stable at certain pressure ranges. The B covalent networks are evolved from 6-atom B octahedrons in *Pm*-3*m* to 24-atom B units in *I*4/*mmm*. The predicted high-pressure phases are dynamically stable at ambient and high pressure based on the calculated phonon spectra. The chemical bonding analysis found that the B−B bonds in *Cmcm* and *I*4/*mmm* phase are longer than those in ambient-pressure phase of *Pm*-3*m* structure. Electronic structure calculations show that both high-pressure phases are metallic with similar electronic states at Fermi level with the *Pm*-3*m* structure. Further electron−phonon coupling analyses indicate that the contribution of Y and B phonon vibrations for the electron−phonon coupling are increased and decreased in *Cmcm* and *I*4/*mmm* phases, respectively, contrary to that in the *Pm*-3*m* phase. The calculated superconductive critical temperatures for *Cmcm* and *I*4/*mmm* phases are 2.00 K at 5 GPa and 3.75 K at 37 GPa, respectively. Our study may stimulate the future high-pressure experiments on the structural and superconductivity measurements of YB_6. Furthermore, our results provide useful knowledge for the high-pressure behavior of metal hexaborides family.

AUTHOR INFORMATION

Corresponding Authors

*E-mail: liquan777@jlu.edu.cn.

*E-mail: gaobo@calypso.cn.

ORCID

Quan Li: 0000-0002-7724-1289

Notes

The authors declare no competing financial interest.

ACKNOWLEDGMENTS

This work was supported by the National Natural Science Foundation of China under Grant Nos. 11622432, 11474125, and 11534003; the National Key Research and Development Program of China under Grant No. 2016YFB0201200; the 2012 Changjiang Scholars Program of China; and Program for JLU Science and Technology Innovative Research Team. Part of the calculation was performed in the high-performance computing center of Jilin University and at Tianhe2-JK in the Beijing Computational Science Research Center.

REFERENCES

(1) Cahill, J. T.; Alberga, M.; Bahena, J.; Pisano, C.; Borja-Urby, R.; Vasquez, V. R.; Edwards, D.; Misture, S. T.; Graeve, O. A. Phase Stability of Mixed-Cation Alkaline-Earth Hexaborides. *Cryst. Growth Des.* **2017**, *17* (6), 3450−3461.

(2) Cahill, J. T.; Vasquez, V. R.; Misture, S. T.; Edwards, D.; Graeve, O. A. Effect of Current on Diffusivity in Metal Hexaborides: a Spark Plasma Sintering Study. *ACS Appl. Mater. Interfaces* **2017**, *9* (42), 37357−37363.

(3) Schmidt, K. M.; Graeve, O. A.; Vasquez, V. R. Ab Initio and Molecular Dynamics-Based Pair Potentials for Lanthanum Hexaboride. *J. Phys. Chem. C* **2015**, *119* (25), 14288−14296.

(4) Young, D. P.; Hall, D.; Torelli, M. E.; Fisk, Z.; Sarrao, J. L.; Thompson, J. D.; Ott, H. R.; Oseroff, S. B.; Goodrich, R. G.; Zysler, R. High-Temperature Weak Ferromagnetism in a Low-Density Free-Electron Gas. *Nature* **1999**, *397* (6718), 412−414.

(5) Monnier, R.; Delley, B. Point Defects, Ferromagnetism, and Transport in Calcium Hexaboride. *Phys. Rev. Lett.* **2001**, *87* (15), 157204.

DOI: 10.1021/acs.jpcc.8b08017
J. Phys. Chem. C 2018, 122, 27820−27828

(6) Rhyee, J.-S.; Cho, B. K. The Effect of Boron Purity on Electric and Magnetic Properties of CaB_6. *J. Appl. Phys.* **2004**, *95* (11), 6675−6677.
(7) Joss, W.; van Ruitenbeek, J. M.; Crabtree, G. W.; Tholence, J. L.; van Deursen, A. P. J.; Fisk, Z. Observation of the Magnetic Field Dependence of the Cyclotron Mass in the Kondo Lattice CeB6. *Phys. Rev. Lett.* **1987**, *59* (14), 1609−1612.
(8) Degiorgi, L.; Felder, E.; Ott, H. R.; Sarrao, J. L.; Fisk, Z. Low-Temperature Anomalies and Ferromagnetism of EuB6. *Phys. Rev. Lett.* **1997**, *79* (25), 5134−5137.
(9) Neupane, M.; Alidoust, N.; Xu, S.-Y.; Kondo, T.; Ishida, Y.; Kim, D. J.; Liu, C.; Belopolski, I.; Jo, Y. J.; Chang, T.-R.; et al. Surface Electronic Structure of the Topological Kondo-Insulator Candidate Correlated Electron System SmB6. *Nat. Commun.* **2013**, *4* (2991), 1−7.
(10) Miyazaki, H.; Hajiri, T.; Ito, T.; Kunii, S.; Kimura, S.-I. Momentum-Dependent Hybridization Gap and Dispersive in-Gap State of the Kondo Semiconductor SmB6. *Phys. Rev. B: Condens. Matter Mater. Phys.* **2012**, *86* (7), 075105.
(11) Weng, H.; Zhao, J.; Wang, Z.; Fang, Z.; Dai, X. Topological Crystalline Kondo Insulator in Mixed Valence Ytterbium Borides. *Phys. Rev. Lett.* **2014**, *112* (1), 016403.
(12) Neupane, M.; Xu, S.-Y.; Alidoust, N.; Bian, G.; Kim, D. J.; Liu, C.; Belopolski, I.; Chang, T.-R.; Jeng, H.-T.; Durakiewicz, T.; et al. Non-Kondo-Like Electronic Structure in the Correlated Rare-Earth Hexaboride YbB6. *Phys. Rev. Lett.* **2015**, *114* (1), 016403.
(13) Singh, P. P. From *E2G* To Other Modes: Effects of Pressure on Electron-Phonon Interaction in MgB2. *Phys. Rev. Lett.* **2006**, *97* (24), 247002.
(14) Ma, Y.; Wang, Y.; Oganov, A. R. Absence of Superconductivity in the High-Pressure Polymorph of MgB_2. *Phys. Rev. B: Condens. Matter Mater. Phys.* **2009**, *79* (5), 054101−054105.
(15) Wang, Y.; Lv, J.; Ma, Y.; Cui, T.; Zou, G. Superconductivity of MgB2 Under Ultrahigh Pressure: a First-Principles Study. *Phys. Rev. B: Condens. Matter Mater. Phys.* **2009**, *80* (9), 092505.
(16) Alarco, J. A.; Talbot, P. C.; Mackinnon, I. D. R. Electron Density Response to Phonon Dynamics in MgB2: An Indicator of Superconducting Properties. *Model. Numer. Simul. Mater. Sci.* **2018**, *08* (02), 21−46.
(17) Lortz, R.; Wang, Y.; Tutsch, U.; Abe, S.; Meingast, C.; Popovich, P.; Knafo, W.; Shitsevalova, N.; Paderno, Y. B.; Junod, A. Superconductivity Mediated by a Soft Phonon Mode: Specific Heat, Resistivity, Thermal Expansion, and Magnetization of YB6. *Phys. Rev. B: Condens. Matter Mater. Phys.* **2006**, *73* (2), 2004−2013.
(18) Shein, I. R.; Okatov, S. V.; Medvedeva, N. I.; Ivanovskii, A. L. Electronic Band Structure of Low-Temperature YB12, Yb6 Superconductors and Layered YB2, MgB2 Diborides. 2002, arXiv preprint cond-mat/0202015.
(19) Zhou, D.; Li, Q.; Ma, Y.; Cui, Q.; Chen, C. Pressure-Induced Superconductivity in SnTe: a First-Principles Study. *J. Phys. Chem. C* **2013**, *117* (23), 12266−12271.
(20) Zhang, S.; Lin, J.; Wang, Y.; Yang, G.; Bergara, A.; Ma, Y. Nonmetallic FeH6 Under High Pressure. *J. Phys. Chem. C* **2018**, *122* (22), 12022−12028.
(21) Luo, D.; Wang, Y.; Yang, G.; Ma, Y. Barium in High Oxidation States in Pressure-Stabilized Barium Fluorides. *J. Phys. Chem. C* **2018**, *122* (23), 12448−12453.
(22) Peng, F.; Botana, J.; Wang, Y.; Ma, Y.; Miao, M. Unexpected Trend in Stability of Xe−F Compounds Under Pressure Driven by Xe−Xe Covalent Bonds. *J. Phys. Chem. Lett.* **2016**, *7* (22), 4562−4567.
(23) Zhang, Y.; Wu, W.; Wang, Y.; Yang, S. A.; Ma, Y. Pressure-Stabilized Semiconducting Electrides in Alkaline-Earth-Metal Subnitrides. *J. Am. Chem. Soc.* **2017**, *139* (39), 13798−13803.
(24) Xu, Y.; Zhang, L.; Cui, T.; Li, Y.; Xie, Y.; Yu, W.; Ma, Y.; Zou, G. First-Principles Study of the Lattice Dynamics, Thermodynamic Properties and Electron-Phonon Coupling of YB_6. *Phys. Rev. B: Condens. Matter Mater. Phys.* **2007**, *76* (21), 359.
(25) Sluchanko, N.; Glushkov, V.; Demishev, S.; Azarevich, A.; Anisimov, M.; Bogach, A.; Voronov, V.; Gavrilkin, S.; Mitsen, K.; Kuznetsov, A.; et al. Lattice Instability and Enhancement of Superconductivity in YB_6. *Phys. Rev. B: Condens. Matter Mater. Phys.* **2017**, *96* (14), 816−818.
(26) Gabáni, S.; Takáčová, I.; Pristáš, G.; Gažo, E.; Flachbart, K.; Mori, T.; Braithwaite, D.; Míšek, M.; Kamenev, K. V.; Hanfland, M.; et al. High-Pressure Effect on the Superconductivity of YB_6. *Phys. Rev. B: Condens. Matter Mater. Phys.* **2014**, *90* (4), 045136−045137.
(27) Peng, F.; Sun, Y.; Pickard, C. J.; Needs, R. J.; Wu, Q.; Ma, Y. Hydrogen Clathrate Structures in Rare Earth Hydrides at High Pressures: Possible Route to Room-Temperature Superconductivity. *Phys. Rev. Lett.* **2017**, *119* (10), 966.
(28) Kolmogorov, A. N.; Shah, S.; Margine, E. R.; Kleppe, A. K.; Jephcoat, A. P. Pressure-Driven Evolution of the Covalent Network in CaB6. *Phys. Rev. Lett.* **2012**, *109* (7), 075501.
(29) Li, X.; Huang, X.; Duan, D.; Wu, G.; Liu, M.; Zhuang, Q.; Wei, S.; Huang, Y.; Li, F.; Zhou, Q.; et al. The Stability of B_6 Octahedron in BaB_6 Under High Pressure. *RSC Adv.* **2016**, *6*, 18077−18081.
(30) Teredesai, P.; Muthu, D. V. S.; Chandrabhas, N.; Meenakshi, S.; Vijayakumar, V.; Modak, P.; Rao, R. S.; Godwal, B. K.; Sikka, S. K.; Sood, A. K. High Pressure Phase Transition in Metallic LaB_6: Raman and X-Ray Diffraction Studies. *Solid State Commun.* **2004**, *129* (12), 791−796.
(31) Wang, Y.; Lv, J.; Zhu, L.; Ma, Y. Crystal Structure Prediction via Particle-Swarm Optimization. *Phys. Rev. B: Condens. Matter Mater. Phys.* **2010**, *82* (9), 094116.
(32) Wang, Y.; Lv, J.; Zhu, L.; Ma, Y. CALYPSO: a Method for Crystal Structure Prediction. *Comput. Phys. Commun.* **2012**, *183* (10), 2063−2070.
(33) Li, Y.; Feng, X.; Liu, H.; Hao, J.; Redfern, S. A. T.; Lei, W.; Liu, D.; Ma, Y. Route to High-Energy Density Polymeric Nitrogen T-N via He-N Compounds. *Nat. Commun.* **2018**, *9* (772), 1−7.
(34) Lv, J.; Xu, M.; Lin, S.; Shao, X.; Zhang, X.; Liu, Y.; Wang, Y.; Chen, Z.; Ma, Y. Direct-Gap Semiconducting Tri-Layer Silicene with 29% Photovoltaic Efficiency. *Nano Energy* **2018**, *51*, 489−495.
(35) Lv, J.; Wang, Y.; Zhu, L.; Ma, Y. Predicted Novel High-Pressure Phases of Lithium. *Phys. Rev. Lett.* **2011**, *106* (1), 015503−015504.
(36) Zhu, L.; Liu, H.; Pickard, C. J.; Zou, G.; Ma, Y. Reactions of Xenon with Iron and Nickel Are Predicted in the Earth's Inner Core. *Nat. Chem.* **2014**, *6* (7), 644−648.
(37) Zhu, L.; Wang, H.; Wang, Y.; Lv, J.; Ma, Y.; Cui, Q.; Ma, Y.; Zou, G. Substitutional Alloy of Bi and Te at High Pressure. *Phys. Rev. Lett.* **2011**, *106* (14), 2051−2054.
(38) Li, Q.; Zhou, D.; Zheng, W.; Ma, Y.; Chen, C. Global Structural Optimization of Tungsten Borides. *Phys. Rev. Lett.* **2013**, *110* (13), 136403−136405.
(39) Zhang, M.; Liu, H.; Li, Q.; Gao, B.; Wang, Y.; Li, H.; Chen, C.; Ma, Y. Superhard BC3 In Cubic Diamond Structure. *Phys. Rev. Lett.* **2015**, *114* (1), 015502−015505.
(40) Li, Q.; Zhou, D.; Zheng, W.; Ma, Y.; Chen, C. Anomalous Stress Response of Ultrahard WBn Compounds. *Phys. Rev. Lett.* **2015**, *115* (18), 185502−185505.
(41) Zhou, D.; Li, Q.; Ma, Y.; Cui, Q.; Chen, C. Pressure-Induced Superconductivity in SnTe: a First-Principles Study. *J. Phys. Chem. C* **2013**, *117* (23), 12266−12271.
(42) Lu, C.; Li, Q.; Ma, Y.; Chen, C. Extraordinary Indentation Strain Stiffening Produces Superhard Tungsten Nitrides. *Phys. Rev. Lett.* **2017**, *119* (11), 115503−115506.
(43) Lu, C.; Chen, C. High-Pressure Evolution of Crystal Bonding Structures and Properties of FeOOH. *J. Phys. Chem. Lett.* **2018**, *9* (9), 2181−2185.
(44) Lu, C.; Amsler, M.; Chen, C. Unraveling the Structure and Bonding Evolution of the Newly Discovered Iron Oxide FeO2. *Phys. Rev. B: Condens. Matter Mater. Phys.* **2018**, *98* (5), 054102.
(45) Su, C.; Lv, J.; Li, Q.; Wang, H.; Zhang, L.; Wang, Y.; Ma, Y. Construction of Crystal Structure Prototype Database: Methods and Applications. *J. Phys.: Condens. Matter* **2017**, *29* (16), 165901−165911.

DOI: 10.1021/acs.jpcc.8b08017
J. Phys. Chem. C 2018, 122, 27820−27828

(46) Kresse, G.; Furthmüller, J. Efficient Iterative Schemes for Ab Initio Total-Energy Calculations Using a Plane-Wave Basis Set. *Phys. Rev. B: Condens. Matter Mater. Phys.* **1996**, *54* (16), 11169−11186.
(47) Blochl, P. E. Projector Augmented-Wave Method. *Phys. Rev. B: Condens. Matter Mater. Phys.* **1994**, *50* (24), 17953−17979.
(48) Kresse, G.; Joubert, D. From Ultrasoft Pseudopotentials to the Projector Augmented-Wave Method. *Phys. Rev. B: Condens. Matter Mater. Phys.* **1999**, *59* (3), 1758−1775.
(49) Perdew, J. P.; Burke, K.; Ernzerhof, M. Generalized Gradient Approximation Made Simple. *Phys. Rev. Lett.* **1996**, *77* (18), 3865−3868.
(50) Monkhorst, H. J.; Pack, J. D. Special Points for Brillouin-Zone Integrations. *Phys. Rev. B* **1976**, *13* (12), 5188−5192.
(51) Parlinski, K.; Li, Z. Q.; Kawazoe, Y. First-Principles Determination of the Soft Mode in Cubic ZrO2. *Phys. Rev. Lett.* **1997**, *78* (21), 4063−4066.
(52) Togo, A.; Oba, F.; Tanaka, I. First-Principles Calculations of the Ferroelastic Transition Between Rutile-Type and $CaCl_2$-Type SiO_2 at High Pressures. *Phys. Rev. B: Condens. Matter Mater. Phys.* **2008**, *78* (13), 693−699.
(53) Bader, R. F. W. Atoms in Molecules. *Acc. Chem. Res.* **1985**, *18* (1), 9−15.
(54) Giannozzi, P.; Baroni, S.; Bonini, N.; Calandra, M.; Car, R.; Cavazzoni, C.; Ceresoli, D.; Chiarotti, G. L.; Cococcioni, M.; Dabo, I.; et al. QUANTUM ESPRESSO: a Modular and Open-Source Software Project for Quantum Simulations of Materials. *J. Phys.: Condens. Matter* **2009**, *21* (39), 395502−395520.
(55) Bando, H.; Hasegawa, T.; Ogita, N.; Udagawa, M.; Iga, F. Raman Scattering of YB6. *J. Phys. Soc. Jpn.* **2011**, *80*, SA053.
(56) Ponosov, Y. S.; Shitsevalova, N. Y. Phonons in YB6 And LaB6: Effects of Temperature and Pressure. *JETP Lett.* **2015**, *102* (5), 295−300.
(57) Orendáč, M.; Gabáni, S.; Gažo, E.; Pristáš, G.; Flachbart, K.; Mori, T.; Wang, X.; Kamenev, K. Pressure Effect on the Einstein-Like Phonon Mode in Superconducting. *J. Low Temp. Phys.* **2017**, *187* (5), 553−558.
(58) Alarco, J. A.; Shahbazi, M.; Talbot, P. C.; Mackinnon, I. D. R. Spectroscopy of Metal Hexaborides: Phonon Dispersion Models. *J. Raman Spectrosc.* **2018**, *3* (4), 158.
(59) Shah, S.; Kolmogorov, A. N. Stability and Superconductivity of Ca-B Phases at Ambient and High Pressure. *Phys. Rev. B: Condens. Matter Mater. Phys.* **2013**, *88*, 014107.
(60) Zhou, Y.; Liu, B.; Xiang, H.; Feng, Z.; Li, Z. YB_6: a "Ductile" and Soft Ceramic with Strong Heterogeneous Chemical Bonding for Ultrahigh-Temperature Applications. *Mater. Res. Lett.* **2015**, *3* (4), 210−215.
(61) Zhou, Y.; Dai, F.; Xiang, H.; Liu, B.; Feng, Z. Shear Anisotropy: Tuning High Temperature Metal Hexaborides From Soft to Extremely Hard. *J. Mater. Sci. Technol.* **2017**, *33* (11), 1371−1377.
(62) Zhou, D.; Li, Q.; Zheng, W.; Ma, Y.; Chen, C. Structural Metatransition of Energetically Tangled Crystalline Phases. *Phys. Chem. Chem. Phys.* **2017**, *19*, 4560−4566.
(63) Kolmogorov, A. N.; Shah, S.; Margine, E. R.; Bialon, A. F.; Hammerschmidt, T.; Drautz, R. New Superconducting and Semiconducting Fe-B Compounds Predicted with an Ab Initio Evolutionary Search. *Phys. Rev. Lett.* **2010**, *105* (21), 120−124.
(64) Liu, C.; Zhai, H.; Sun, Y.; Gong, W.; Yan, Y.; Li, Q.; Zheng, W. Strain-Induced Modulations of Electronic Structure and Electron−Phonon Coupling in Dense H3S. *Phys. Chem. Chem. Phys.* **2018**, *20* (8), 5952−5957.

DOI: 10.1021/acs.jpcc.8b08017
J. Phys. Chem. C 2018, 122, 27820−27828